The Astrophysical Journal Letters, 996:L13 (14pp), 2026 January 1 https://doi.org/10.3847/2041-8213/ae2bfa

A Cold and Superpuffy Planet on a Prograde Orbit

Juan I. Espinoza-Retamal[1,2,3], Rafael Brahm[3,4], Cristobal Petrovich[5], Andrés Jordán[3,4,6], Thomas Henning[7], Trifon Trifonov[7,8,9], Joshua N. Winn[1], Erika Rea[10], Maximilian N. Günther[10], Abdelkrim Agabi[11], Philippe Bendjoya[11], Hareesh Bhaskar[5], François Bouchy[12], Márcio Catelan[2,3], Carolina Charalambous[2], Vincent Deloupy[13], George Dransfield[14,15,16], Jan Eberhardt[7], Néstor Espinoza[17], Alix V. Freckelton[14], Tristan Guillot[11], Melissa J. Hobson[12], Matías I. Jones[18], Monika Lendl[12], Djamel Mekarnia[11], Diego J. Muñoz[19], Louise D. Nielsen[12,20], Felipe I. Rojas[2], François-Xavier Schmider[11], Elyar Sedaghati[18], Guđmundur Stefánsson[21], Stephanie Striegel[22,23], Olga Suarez[11], Marcelo Tala Pinto[24], Mathilde Timmermans[14], Amaury H. M. J. Triaud[14], Stéphane Udry[12], Solène Ulmer-Moll[12,25], and Carl Ziegler[26]

[1] Department of Astrophysical Sciences, Princeton University, 4 Ivy Lane, Princeton, NJ 08540, USA; jiespinozar@princeton.edu
[2] Instituto de Astrofísica, Pontificia Universidad Católica de Chile, Av. Vicuña Mackenna 4860, 7820436 Macul, Santiago, Chile
[3] Millennium Institute for Astrophysics, Nuncio Monseñor Sotero Sanz 100, Of. 104, 7500011 Providencia, Santiago, Chile
[4] Facultad de Ingeniería y Ciencias, Universidad Adolfo Ibáñez, Av. Diagonal las Torres 2640, 7941169 Peñalolén, Santiago, Chile
[5] Department of Astronomy, Indiana University, Bloomington, IN 47405, USA
[6] Data Observatory Foundation, Av. Eliodoro Yáñez 2990, 7510277 Providencia, Santiago, Chile
[7] Max-Planck-Institut für Astronomie, Königstuhl 17, D-69117 Heidelberg, Germany
[8] Department of Astronomy, Sofia University "St Kliment Ohridski," 5 James Bourchier Blvd, BG-1164 Sofia, Bulgaria
[9] Landessternwarte, Zentrum für Astronomie der Universität Heidelberg, Königstuhl 12, D-69117 Heidelberg, Germany
[10] European Space Agency (ESA), European Space Research and Technology Centre (ESTEC), Keplerlaan 1, 2201 AZ Noordwijk, The Netherlands
[11] Université Côte d'Azur, Observatoire de la Côte d'Azur, CNRS, Laboratoire Lagrange, CS 34229, F-06304 Nice Cedex 4, France
[12] Observatoire de Genève, Département d'Astronomie, Université de Genève, Chemin Pegasi 51b, 1290 Versoix, Switzerland
[13] École Normale Supérieure, Département de Physique, Rue d'Ulm, 75005, Paris Cedex 5, France
[14] School of Physics & Astronomy, University of Birmingham, Edgbaston, Birmingham B15 2TT, UK
[15] Department of Astrophysics, University of Oxford, Denys Wilkinson Building, Keble Road, Oxford OX1 3RH, UK
[16] Magdalen College, University of Oxford, Oxford OX1 4AU, UK
[17] Space Telescope Science Institute, 3700 San Martin Drive, Baltimore, MD 21218, USA
[18] European Southern Observatory (ESO), Alonso de Córdova 3107, Vitacura, Casilla 19001, Santiago, Chile
[19] Department of Astronomy and Planetary Science, Northern Arizona University, Flagstaff, AZ 86011, USA
[20] University Observatory, Faculty of Physics, Ludwig-Maximilians-Universität München, Scheinerstr. 1, 81679 Munich, Germany
[21] Anton Pannekoek Institute for Astronomy, University of Amsterdam, Science Park 904, 1098 XH Amsterdam, The Netherlands
[22] SETI Institute, Mountain View, CA 94043, USA
[23] NASA Ames Research Center, Moffett Field, CA 94035, USA
[24] Department of Astronomy, McPherson Laboratory, The Ohio State University, 140 W 18th Ave, Columbus, OH 43210, USA
[25] Leiden Observatory, Leiden University, P.O. Box 9513, 2300 RA Leiden, The Netherlands
[26] Department of Physics, Engineering and Astronomy, Stephen F. Austin State University, 1936 North St, Nacogdoches, TX 75962, USA

Received 2025 September 30; revised 2025 November 26; accepted 2025 December 8; published 2025 December 30

Abstract

We report the discovery of TOI-4507 b, a transiting sub-Saturn with a density $<0.2\,\mathrm{g\,cm^{-3}}$ on a 105 days prograde orbit around a 700 Myr old F star. The transits were detected using data from TESS as well as the Antarctic telescope ASTEP. A joint analysis of the light curves and radial velocities from HARPS, FEROS, and CORALIE confirmed the planetary nature of the signal, by limiting the mass to be below $20\,M_\oplus$ at 95% confidence. The radial velocities also exhibit the Rossiter–McLaughlin effect and imply that the planet orbits the star in a prograde orbit with a sky-projected obliquity $\lambda = -15^{+50\circ}_{-44}$ ($|\lambda| < 80^\circ$ at 3σ). With these characteristics, TOI-4507 is one of the longest-period systems for which the stellar obliquity has been measured, and the planet is among the longest-period and youngest "superpuff" planets yet discovered.

Unified Astronomy Thesaurus concepts: Transit photometry (1709); Exoplanets (498); Radial velocity (1332); Cold Neptunes (2132)

Materials only available in the online version of record: machine-readable table

1. Introduction

More than 6000 exoplanets have been discovered,[27] most of them using the methods of transits and radial velocities (RVs). The Kepler (W. J. Borucki et al. 2010) and Transiting Exoplanet Survey Satellite (TESS; G. R. Ricker et al. 2015) discoveries have revealed valuable information about the demographics of short-period exoplanets (see, e.g., a review by W. Zhu & S. Dong 2021). However, because the probability of observing transits decreases with orbital distance, it is challenging to explore the outer regions of planetary systems using transits (e.g., B. S. Gaudi et al. 2005). Likewise, RV surveys have revealed valuable information about the demographics of cold Jupiters (e.g., A. Cumming et al. 2008; R. A. Wittenmyer et al. 2016; R. B. Fernandes et al. 2019;

---

[27] https://exoplanetarchive.ipac.caltech.edu/

A. S. Bonomo et al. 2023), but because the RV semiamplitude decreases with decreasing planetary mass and increasing semimajor axis, it has been difficult to study less massive cold worlds.

Interestingly, recent discoveries have uncovered the existence of the so-called "superpuff" exoplanets (e.g., K. Masuda 2014; A. Santerne et al. 2019; K. Barkaoui et al. 2024), which have sizes comparable to that of Jupiter but masses less than that of Saturn or even comparable to that of Neptune, leading to mean densities $\lesssim 0.3$ g cm^{-3}. Possible explanations for these low densities involve the accretion of unusually thick H/He envelopes under conditions that enable rapid cooling, such as dust-free formation beyond 1 au followed by inward migration (e.g., E. J. Lee & E. Chiang 2016) or inflation due to tidal dissipation (e.g., S. Millholland 2019; S. Millholland et al. 2020; R. Sethi & S. Millholland 2025). It is also possible that some planets with apparently low densities are actually normal planets with large opaque rings (e.g., B. Akinsanmi et al. 2020; M. Saillenfest et al. 2023; T. Lu et al. 2025)—a hypothesis that has been explored in detail for HIP-41378 f (A. Vanderburg et al. 2016; A. Santerne et al. 2019).

In this Letter, we present the discovery and characterization of TOI-4507 b—a cold planet transiting a young F star with an orbital period of 105 days. Our observations reveal that the planet has an unusually low density, making it one of the longest-period superpuffs known to date. Furthermore, our analysis of the Rossiter–McLaughlin (RM) effect (D. McLaughlin 1924; R. Rossiter 1924) shows that the planet has a prograde orbit, making it one of the longest-period systems for which the stellar obliquity has been measured. A more detailed validation of TOI-4507 b using TESS and Antarctic Search for Transiting ExoPlanets (ASTEP) data appears in a separate paper (E. Rea et al. 2025).

2. Observations

2.1. Photometry

2.1.1. TESS

Between 2018 and 2024, TOI-4507 was observed by TESS in Sectors 2, 3, 5–13, 27–30, 32–39, 61–69, and 87–89, and all of the data are available with 2 minutes time sampling. The TESS Science Processing Operations Center (SPOC; J. M. Jenkins et al. 2016) pipeline identified a transit signal with a periodicity of 105 days and a depth of 6100 ppm. We downloaded and combined all the available light curves using the code provided by the Lightkurve Collaboration et al. (2018). We used the Presearch Data Conditioning Simple Aperture Photometry SPOC light curves (J. C. Smith et al. 2012; M. C. Stumpe et al. 2012, 2014), which are corrected for pointing and focus-related instrumental signatures, discontinuities resulting from radiation events in the CCD detectors, outliers, and contributions to the recorded flux from nearby stars. The TESS light curve, along with the best transit model, are shown in Figure 1.

2.1.2. ASTEP

We followed up the TESS observations using photometry from the ground. We observed one transit egress on 2023 May 23 and one full transit on 2025 May 24, using the ASTEP 0.4 m telescope (T. Guillot et al. 2015; D. Mékarnia et al. 2016) located at Concordia station in Antarctica. Observations were performed simultaneously in the R and B bands, however, the observations of the 2025 transit are only available in the R band, due to a technical issue. The ASTEP data were processed on site using a combination of `IDL` and `python` aperture photometry pipelines (e.g., L. Abe et al. 2013; D. Mékarnia et al. 2016; G. Dransfield et al. 2022). The resulting light curves, along with the best models, are shown in Figure 1. A more detailed validation of TOI-4507 b using TESS and ASTEP data is presented in a separate paper (E. Rea et al. 2025).

2.2. Spectroscopy

2.2.1. High Accuracy Radial Velocity Planet Searcher

In order to confirm the planetary nature of TOI-4507 b, we observed the target with the High Accuracy Radial velocity Planet Searcher (HARPS) spectrograph (M. Mayor et al. 2003) installed on the ESO 3.6 m telescope at La Silla observatory, Chile. HARPS is an echelle spectrograph with a resolving power of $R \approx 115{,}000$, which covers the wavelength range of 380–690 nm. We obtained a total of 31 out-of-transit spectra between 2019 October and 2025 March in the context of the Warm gIaNts with tEss collaboration (e.g., R. Brahm et al. 2023; J. Eberhardt et al. 2025; M. Tala Pinto et al. 2025; M. Vítková et al. 2025), whose main objective is to detect and characterize relatively long-period transiting exoplanets. The exposure times range between 1200 s and 1500 s, contingent upon prevailing sky and seeing conditions.

In addition to the out-of-transit HARPS observations, we observed about 70% of a transit of TOI-4507 b on 2024 October 27, between 02:18 and 08:48 UTC. We obtained 20 spectra of the host star during the transit, with an exposure time of 1200 s. The observations were performed under clear sky conditions, with a median atmospheric seeing of $1\farcs3$ and airmass varying from 2.0 to 1.3.

The spectra were reduced using the `ceres` pipeline (R. Brahm et al. 2017a), which, starting from the raw images, performs all reduction steps and derives precise RVs via the cross-correlation-function (CCF) technique. The median signal-to-noise ratio (S/N) of the processed spectra is 50 per resolution element at 550 nm, leading to a median formal RV uncertainty of 4.7 m s^{-1}. Because of the warm up of HARPS on 2020 March 23, due to the COVID-19 pandemic, the data taken before and after this date were considered as having come from different instruments (HARPS1 and HARPS2), with different additive RV offsets and "jitter" parameters (the level of uncertainty in excess of the formal uncertainty). The HARPS RVs of the target, together with the best model, are shown in Figure 1 and available in Appendix A.

2.2.2. Fiber-fed Extended Range Optical Spectrograph

We also observed the target using the Fiber-fed Extended Range Optical Spectrograph (FEROS; A. Kaufer et al. 1999) installed in the MPG/ESO 2.2 m telescope in La Silla Observatory in Chile. FEROS is an echelle spectrograph with a resolving power of $R \approx 48{,}000$ and a wavelength-range coverage of 350–920 nm. We obtained a total of 11 out-of-transit spectra of the star between 2019 August and 2023 November. The exposure times range between 600 s and 1800 s. FEROS observations were also processed using the `ceres` pipeline and RVs extracted using the CCF method. The median S/N of the FEROS spectra is 95 per resolution element at 550 nm, with a median RV uncertainty of 9.5 m s^{-1}. The

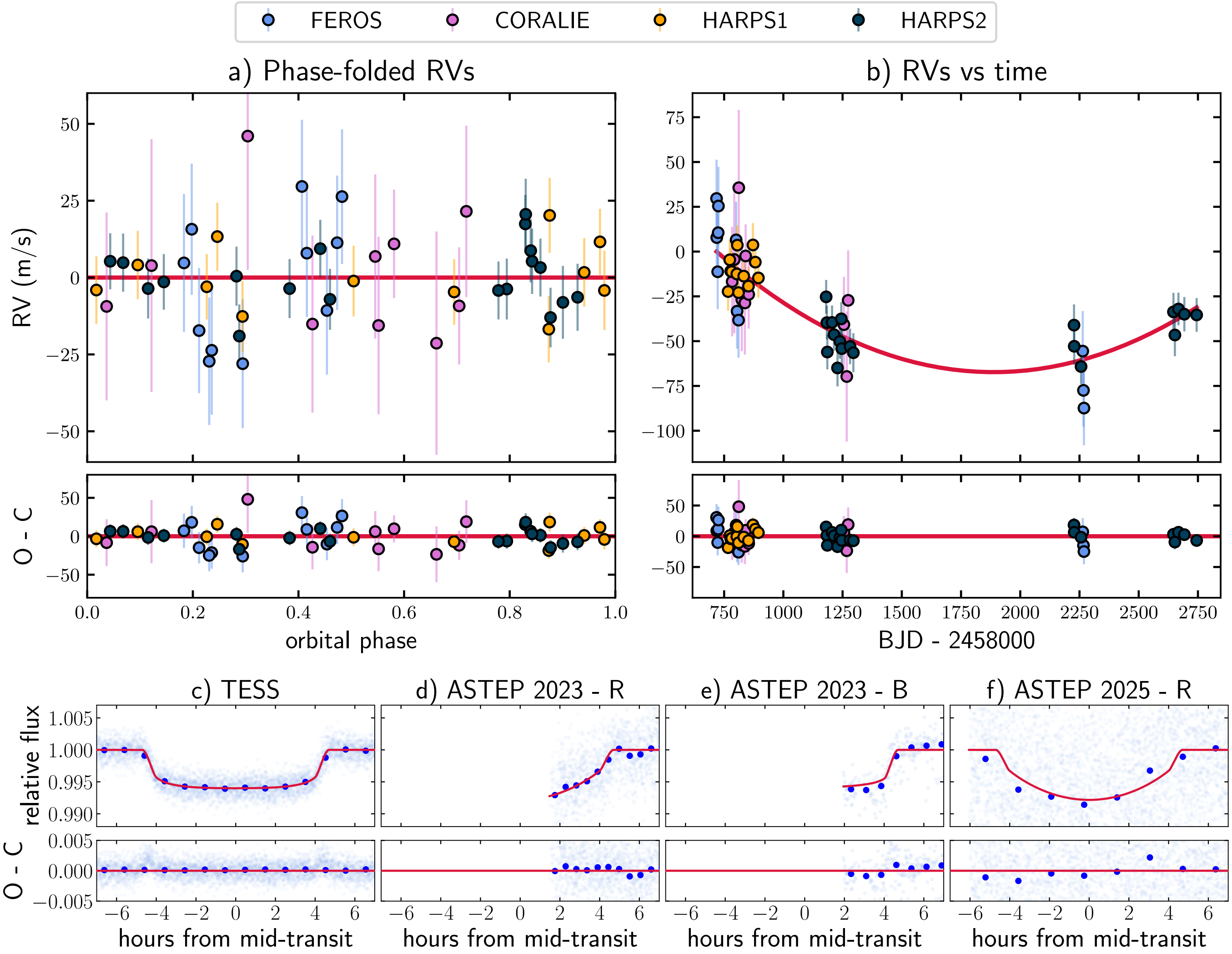

Figure 1. Different observations of TOI-4507 along with the best model. (a) Phase-folded out-of-transit RVs taken with different instruments, along with the best model in red. (b) RVs as a function of time showing the long-term trend detected at a 5σ confidence level. (c)–(f) Different light curves along with the best model. Binned data are shown as the solid blue points.

resulting FEROS RVs for TOI-4507, along with the best-fit model, are presented in Figure 1 and available in Appendix A.

2.2.3. *CORALIE*

We also observed the target using the CORALIE spectrograph (D. Queloz et al. 2001) installed in the Swiss 1.2 m Leonhard Euler Telescope at ESO's La Silla Observatory. CORALIE is an echelle spectrograph with a resolving power of $R \approx 60{,}000$, which covers the wavelength range of 390–680 nm. We observed TOI-4507 using exposure times varying between 900 and 1800 s, together with the simultaneous Fabry-Pérot etalon. We obtained a total of 10 out-of-transit spectra between 2019 October and 2021 February. Data reduction was done using the dedicated CORALIE data reduction pipeline, which also derives RVs using the CCF technique and a G2 mask. The CORALIE observations have a median RV uncertainty of 28 m s^{-1} and are shown in Figure 1, along with the best model. The data are available in Appendix A.

2.3. *High-resolution Imaging*

In order to search for nearby sources that may contaminate the TESS photometry, resulting in an underestimated planetary radius, or acting as astrophysical false positives, such as background eclipsing binaries, we took a high-resolution image of the target. We observed TOI-4507 with the SOuthern Astrophysical Research (SOAR) 4.1 m telescope (T. A. Sebring et al. 2003; A. Tokovinin 2018) on the night of 2021 November 20. This observation was performed using an I filter and is sensitive enough to detect a 7 mag fainter star at an angular distance of 1″ from the target. More details of the observations within the SOAR–TESS survey are available in C. Ziegler et al. (2020). The 5σ detection sensitivity and speckle autocorrelation functions from the observations are shown in Figure 2. No nearby stars were detected within 3″ of TOI-4507 in the SOAR observations.

3. Stellar Characterization

To estimate the stellar parameters of TOI-4507, we followed the two-step iterative procedure presented in R. Brahm et al. (2019). Briefly, in the first step, we computed the stellar atmospheric parameters using the `zaspe` package (R. Brahm et al. 2017b), which compares the coadded high-resolution HARPS spectrum with a grid of synthetic ones to determine the best fit. The search is performed in the spectral regions that

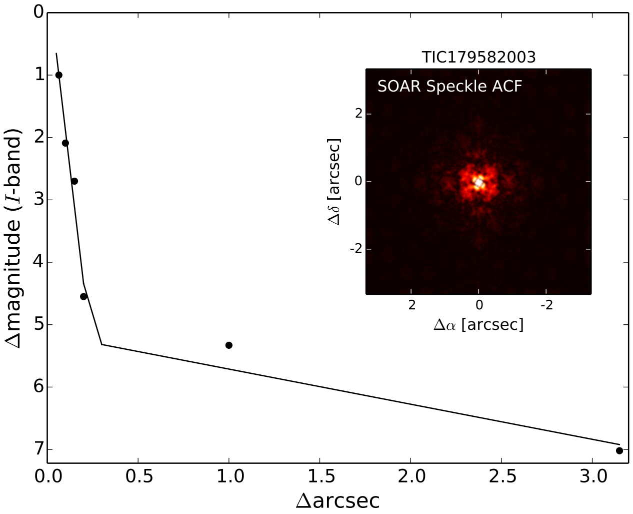

Figure 2. High-resolution imaging observations of TOI-4507 taken with the 4.1 m SOAR telescope. We show the 5σ detection sensitivity and speckle autocorrelation functions. No companions to TOI-4507 within 3″ are found in these observations.

are most sensitive to changes in the stellar parameters, and reliable error bars are computed through Monte Carlo simulations. In the second step, we computed the stellar physical parameters by fitting stellar evolutionary models to the observed spectral energy distribution. We fitted public broadband photometric data to synthetic magnitudes generated from the `PARSEC` isochrones (A. Bressan et al. 2012) and adopting the Gaia Data Release (DR) 3 parallax (Gaia Collaboration et al. 2023). We model interstellar extinction using the prescription of J. A. Cardelli et al. (1989). In this step, the stellar temperature derived with `zaspe` is used as a prior, while the metallicity is held fixed. From the stellar mass and radius obtained with the second step, we obtained a more precise value of $\log g$, which is held fixed in a new iteration of the first step. This procedure is repeated until reaching convergence in $\log g$. The resulting parameters of TOI-4507 are presented in Table 1.

4. Photometric Analysis

To determine the transit ephemerides of TOI-4507 b and look for transit timing variations (TTVs), we analyzed the photometry presented in Section 2 with the `juliet` code (N. Espinoza et al. 2019). This code uses `batman` (L. Kreidberg 2015) for the transit model and the `dynesty` dynamic nested sampler (J. S. Speagle 2020) to sample the posteriors. We placed uniform priors on the impact parameter b and radius ratio $R_p/R_\star$, with a Gaussian prior on the stellar density $\rho_\star$ that was constrained in Section 3. We sampled the limb-darkening parameters using the quadratic q_1 and q_2 parameters from D. M. Kipping (2013) with uniform priors. We placed Gaussian priors for each transit midpoint based on the expected values calculated from the orbital period and time of midtransit from the SPOC solution, placing a large width of 1 day on the prior, to not impact the derived transit midpoints. To account for variability and systematic noise in the TESS light curve, we included a Matern-3/2 Gaussian Process as implemented in `celerite` (D. Foreman-Mackey et al. 2017) and available in `juliet`. From this analysis, we found $P = 104.61573 \pm 0.00008$ days and $t_0 = 2458413.8572 \pm 0.0007$ (BJD). The nearly continuous TESS time series between Sectors 5 and 13, 32 and 39, and 61 and 69 left no doubt that the true orbital period is about 105 days, as consecutive transits are seen in the TESS data. Here, we also obtained a detrended TESS light curve that was used in the subsequent analyses. Finally, we also found tentative evidence for TTVs, as the transit observed with ASTEP in 2025 deviates by $\sim$25 minutes from the linear ephemerides solution. The rest of the transits do not show this behavior, being in all cases within $\sim$5 minutes of the linear solution.

Table 1
Stellar Properties[a] of TOI-4507

Parameter	Description	Value	Reference
R.A.	R.A. (J2015.5)	$05^{\rm h}21^{\rm m}48\overset{\rm s}{.}33$	Gaia DR3[b]
Decl.	decl. (J2015.5)	$-69^{\rm d}59^{\rm m}17\overset{\rm s}{.}58$	Gaia DR3
$\rm pm^{R.A.}$	Proper motion in R.A. (mas yr^{-1})	22.00 ± 0.02	Gaia DR3
$\rm pm^{Decl.}$	Proper motion in Decl. (mas yr^{-1})	3.97 ± 0.02	Gaia DR3
π	Parallax (mas)	5.64 ± 0.01	Gaia DR3
d	Distance (pc)	177.3 ± 0.3	Gaia DR3
T	TESS magnitude (mag)	11.230 ± 0.007	TICv8[c]
B	B-band magnitude (mag)	11.52 ± 0.04	APASS[d]
V	V-band magnitude (mag)	10.806 ± 0.030	APASS
G	Gaia G-band magnitude (mag)	10.567 ± 0.002	Gaia DR3
G_{BP}	Gaia BP-band magnitude (mag)	10.848 ± 0.005	Gaia DR3
G_{RP}	Gaia RP-band magnitude (mag)	10.133 ± 0.003	Gaia DR3
J	2MASS J-band magnitude (mag)	9.69 ± 0.02	2MASS[e]
H	2MASS H-band magnitude (mag)	9.43 ± 0.02	2MASS
K_s	2MASS K_s-band magnitude (mag)	9.38 ± 0.03	2MASS
$T_{\rm eff}$	Effective temperature (K)	6260 ± 80	This work
$\log g$	Surface gravity (cgs)	4.45 ± 0.02	This work
[Fe/H]	Metallicity (dex)	-0.06 ± 0.05	This work
$v \sin i_\star$	Projected rotational velocity (km s^{-1})	4.6 ± 0.9	This work
$M_\star$	Mass ($M_\odot$)	1.11 ± 0.02	This work
$R_\star$	Radius ($R_\odot$)	1.04 ± 0.01	This work
$L_\star$	Luminosity ($L_\odot$)	1.41 ± 0.05	This work
A_V	Visual extinction (mag)	0.07 ± 0.04	This work
Age	Age (Gyr)	$0.7^{+0.8}_{-0.5}$	This work
$\rho_\star$	Density (g cm^{-3})	$1.40^{+0.04}_{-0.05}$	This work

Notes.

[a] The stellar parameters computed in this work do not consider possible systematic differences among different stellar evolutionary models (J. Tayar et al. 2022) and have underestimated uncertainties.

[b] Gaia Collaboration et al. (2023).

[c] K. G. Stassun et al. (2018, 2019). The TESS magnitude is shown only for reference and was not included in our stellar analysis.

[d] U. Munari et al. (2014).

[e] M. F. Skrutskie et al. (2006).

The TESS light curve exhibits a quasiperiodic modulation with a periodicity of $\sim$1.7 days. If this were due to stellar rotation, then the combination of the measurements of the rotation period, stellar radius, and projected rotation velocity would imply a low value of $\sin i_\star \approx 0$ and a nearly polar orbit for the planet. This was our initial interpretation. However, a more detailed analysis revealed that the 1.7 days variability comes from a blended variable star that lies in the background (see Appendix B). Without an estimate of the rotation period of TOI-4507, we cannot constrain the inclination of the stellar rotation axis.

5. Joint Photometric and RV Modeling

In order to derive the parameters of the planet, we performed a joint analysis of all the available photometry and out-of-transit RVs using the `ironman`[28] code (J. I. Espinoza-Retamal et al. 2023a, 2024). In brief, `ironman` is a `python` code that can jointly fit in-transit and out-of-transit RVs together with transit photometry. To model the photometry and RVs, `ironman` uses `radvel` (B. J. Fulton et al. 2018) and `batman` (L. Kreidberg 2015), respectively. Finally, to get the posteriors, `ironman` uses the `dynesty` dynamic nested sampler (J. S. Speagle 2020). A copy of `ironman` version 1.1.0, which was used in the analysis, is available via Zenodo (see J. I. Espinoza-Retamal 2025).

To reduce the computational cost, we only considered the detrended TESS data within 7.5 hr of a transit midpoint. We included independent jitter terms for each RV and photometric instrument, to account for possible instrumental systematics. We placed uniform priors on all of the parameters except for the stellar density, for which we used the constraint described in Section 3. Finally, to account for the possible nondetection of the Keplerian signal in the RVs, we allowed the semiamplitude to take negative values. All priors and resulting posteriors are shown in Table 2.

Figure 1 shows the different datasets along with the best model. We found that TOI-4507 b is comparable to Saturn in size, having a radius of $8.2 \pm 0.1\,R_\oplus$. However, the Keplerian signal was not detected. We found K consistent with 0 m s^{-1}, leading to a 2σ upper limit on the planet's mass of $20\,M_\oplus$, comparable to that of Neptune. This combination results in a bulk density <0.2 g cm^{-3}, making TOI-4507 b a superpuff planet and one of the longest-period planets known to be in this category. Future RV monitoring with more precise instruments will be necessary to precisely measure the mass and density of the planet.

There is a hint of a small eccentricity, $e = 0.09^{+0.26}_{-0.06}$. Indeed, we fitted the data using both a circular and an eccentric model. For the eccentric case, we sampled the eccentricity and argument of periastron as $\sqrt{e}\cos\omega$ and $\sqrt{e}\sin\omega$. The Bayesian evidence difference ($\Delta \log Z$), being <2, is not enough to favor any of the models in particular. As both models returned a fully consistent set of parameters, we elected to formally adopt the values from the eccentric fit, to highlight the possible range of eccentricities compatible with the data. This possible eccentricity can also be further constrained with additional RV measurements.

We found evidence for a long-term RV trend, possibly caused by a longer-period outer companion. We modeled the trend using a quadratic model, $\ddot{\gamma}(t - t_a)^2 + \dot{\gamma}(t - t_a)$, where t_a was arbitrarily chosen to be the time of the earliest precise RV measurement. The fit gave $\ddot{\gamma} = 0.0180 \pm 0.0035$ m s^{-1} day^{-1} yr^{-1} and $\dot{\gamma} = -0.12 \pm 0.02$ m s^{-1} day^{-1}, implying a 5σ detection. Further information about this possible companion, including its orbital inclination, might be found by combining additional RVs and Gaia DR4 astrometry (e.g., J. I. Espinoza-Retamal et al. 2023b), which would help to understand the system's dynamical history.

6. RM Effect

In order to constrain the stellar obliquity, we analyzed the HARPS observations of the RM effect using `ironman`. To model the RM effect, `ironman` uses `rmfit` (G. Stefansson et al. 2020, 2022), which implements the equations from T. Hirano et al. (2010). Given the lack of an estimation of the rotational period of TOI-4507 (see Appendix B), here we only derived the sky-projected obliquity by directly sampling λ and $v \sin i_\star$, both with uninformative uniform priors. We placed informative priors for almost all the rest of the parameters based on the values reported in Table 2. We also placed an informative prior on β, the intrinsic line width accounting for instrumental and macroturbulence broadening. We considered an instrumental broadening of 2.6 km s^{-1}, because of the HARPS resolution, and for the macroturbulence broadening, we followed S. Albrecht et al. (2012) and used the macroturbulence law for hot stars from D. F. Gray (1984), considering $T_{\rm eff} = 6260$ K, which resulted in 5.5 km s^{-1}. We added the instrumental and macroturbulence broadening in quadrature to set our prior, with an uncertainty of 2 km s^{-1}. Finally, to account for possible RV trends in the RM data due to orbital motion or stellar activity, we allowed for an arbitrary RV slope in the model. All priors and resulting posteriors are shown in Table 3.

As shown in Figure 3, we found that TOI-4507 b has a prograde orbit with $\lambda = -15^{+50}_{-44}$ deg. °. Although the reported error bars are relatively large, we show in Appendix C that the posteriors for the sky-projected obliquity are restricted between about −80° and 80°. Thus, the data strongly prefer a prograde orbit.

7. Discussion

7.1. TOI-4507 b in Context

TOI-4507 b appears to be an interesting planet in several ways. Figure 4 shows the results for the projected obliquity λ along with those of other systems. The obliquity data were drawn from TEPCat[29] (J. Southworth 2011), and the age data were drawn from the NASA Exoplanet Archive (R. L. Akeson et al. 2013; J. L. Christiansen et al. 2025), both as of 2025 May. Evidently, TOI-4507 b has one of the longest orbital periods for which λ has been measured, having the fourth-longest orbital period after HIP-41378 d (S. Grouffal et al. 2022), TIC 241249530 b (A. F. Gupta et al. 2024), and HD 80606 b (e.g., G. Hébrard et al. 2010). Here, we define Neptunes/sub-Saturns as the class of planets with $10 < M_p/M_\oplus < 90$, with the subclass of superpuffs having $\rho_p < 0.3$ g cm^{-3}.

TOI-4507 b joins a growing population of Neptune/sub-Saturn systems with measured stellar obliquities (e.g., V. Bourrier et al. 2023; J. I. Espinoza-Retamal et al. 2024; E. Knudstrup et al. 2024; L. B. Handley et al. 2025). This population includes some other superpuffs on prograde orbits, such as K2-261 b (E. Knudstrup et al. 2024), TOI-5398 b (G. Mantovan et al. 2024; B. T. Radzom et al. 2024), WASP-21 b (G. Chen et al. 2020), WASP-39 b (L. Mancini et al. 2018), WASP-69 b (N. Casasayas-Barris et al. 2017), WASP-117 b (M. Lendl et al. 2014), and WASP-193 b

---

[28] https://github.com/jiespinozar/ironman

[29] https://www.astro.keele.ac.uk/jkt/tepcat/

Table 2
Summary of Priors and Posteriors of the Joint Transit Photometry and Out-of-transit-RVs Fit

Parameter	Description	Prior	Posterior
$\rho_\star$	Stellar density (g cm^{-3})	$\mathcal{G}(1.40, 0.05)$	1.41 ± 0.04
P	Orbital period (days)	$\mathcal{U}(104.61493, 104.61653)$[a]	104.61611 ± 0.00006
t_0	Transit midpoint (BJD–2458000)	$\mathcal{U}(413.8472, 413.8612)$[a]	413.8515 ± 0.0008
b	Impact parameter	$\mathcal{U}(0, 1)$	0.12 ± 0.08
i	Orbital inclination (deg)	...	89.93 ± 0.05
$R_p/R_\star$	Radius ratio	$\mathcal{U}(0, 1)$	0.0723 ± 0.0004
$a/R_\star$	Scaled semimajor axis	...	$93.4^{+0.8}_{-0.9}$
K	RV semiamplitude (m s^{-1})	$\mathcal{U}(-100, 100)$	<3 (2σ)
$\sqrt{e}\,\sin\omega$	Eccentricity parameter sine component	$\mathcal{U}(-1, 1)$	$-0.13^{+0.05}_{-0.06}$
$\sqrt{e}\,\cos\omega$	Eccentricity parameter cosine component	$\mathcal{U}(-1, 1)$	$-0.09^{+0.40}_{-0.45}$
e	Eccentricity	...	$0.09^{+0.26}_{-0.06}$
ω	Argument of periastron (deg)	...	-123^{+105}_{-41}
M_p	Planet mass ($M_\oplus$)	...	<20 (2σ)
R_p	Planet radius ($R_\oplus$)	...	8.2 ± 0.1
ρ_p	Planet mean density (g cm^{-3})	...	<0.2 (2σ)
a	Semimajor axis (au)	...	0.456 ± 0.005
$\dot{\gamma}$	RV linear trend (m s^{-1} day^{-1})	$\mathcal{U}(-1, 1)$	-0.12 ± 0.02
$\ddot{\gamma}$	RV quadratic trend (m s^{-1} day^{-1} yr^{-1})	$\mathcal{U}(-1, 1)$	0.0180 ± 0.0035
$\gamma_{\rm HARPS1}$	HARPS1 RV offset (m s^{-1})	$\mathcal{U}(25000, 27000)$	26068 ± 4
$\sigma_{\rm HARPS1}$	HARPS1 RV jitter (m s^{-1})	$\mathcal{LU}(10^{-3}, 100)$	$10.5^{+3.0}_{-2.2}$
$\gamma_{\rm HARPS2}$	HARPS2 RV offset (m s^{-1})	$\mathcal{U}(25000, 27000)$	26095^{+9}_{-10}
$\sigma_{\rm HARPS2}$	HARPS2 RV jitter (m s^{-1})	$\mathcal{LU}(10^{-3}, 100)$	$8.8^{+2.2}_{-1.8}$
$\gamma_{\rm FEROS}$	FEROS RV offset (m s^{-1})	$\mathcal{U}(25000, 27000)$	26065^{+7}_{-8}
$\sigma_{\rm FEROS}$	FEROS RV jitter (m s^{-1})	$\mathcal{LU}(10^{-3}, 100)$	$18.7^{+7.7}_{-5.7}$
$\gamma_{\rm CORALIE}$	CORALIE RV offset (m s^{-1})	$\mathcal{U}(25000, 27000)$	26074 ± 9
$\sigma_{\rm CORALIE}$	CORALIE RV jitter (m s^{-1})	$\mathcal{LU}(10^{-3}, 100)$	$0.1^{+2.3}_{-0.1}$
$q_1^{\rm TESS}$	TESS linear limb-darkening parameter	$\mathcal{U}(0, 1)$	$0.43^{+0.11}_{-0.10}$
$q_2^{\rm TESS}$	TESS quadratic limb-darkening parameter	$\mathcal{U}(0, 1)$	$0.10^{+0.08}_{-0.06}$
$\sigma_{\rm TESS}$	TESS photometric jitter (ppm)	$\mathcal{LU}(1, 5 \times 10^7)$	11^{+54}_{-9}
q_1^R	R linear limb-darkening parameter	$\mathcal{U}(0, 1)$	$0.53^{+0.07}_{-0.06}$
q_2^R	R quadratic limb-darkening parameter	$\mathcal{U}(0, 1)$	$0.92^{+0.06}_{-0.08}$
$\sigma_{\rm ASTEP}^{2023-R}$	ASTEP 2023 R photometric jitter (ppm)	$\mathcal{LU}(1, 5 \times 10^7)$	3070^{+75}_{-78}
$\sigma_{\rm ASTEP}^{2025-R}$	ASTEP 2025 R photometric jitter (ppm)	$\mathcal{LU}(1, 5 \times 10^7)$	8976^{+90}_{-91}
q_1^B	B linear limb-darkening parameter	$\mathcal{U}(0, 1)$	$0.23^{+0.22}_{-0.15}$
q_2^B	B quadratic limb-darkening parameter	$\mathcal{U}(0, 1)$	$0.15^{+0.23}_{-0.11}$
$\sigma_{\rm ASTEP}^{2023-B}$	ASTEP 2023 B photometric jitter (ppm)	$\mathcal{LU}(1, 5 \times 10^7)$	2257^{+103}_{-99}

Note. $\mathcal{U}(a, b)$ denotes a uniform prior with a start value a and end value b. $\mathcal{G}(\mu, \sigma)$ denotes a Gaussian prior with mean μ and standard deviation σ. $\mathcal{LU}(a, b)$ denotes a log-uniform prior with a start value a and end value b.

[a] The priors on the period and midtransit time are uniform between the value $\pm 10\sigma$ based on the values derived in Section 4.

(S. W. Yee et al. 2025). Within this collection of prograde superpuffs, TOI-4507 b has the longest period.

Additionally, with an age of ∼700 Myr, TOI-4507 b is the youngest superpuff with an obliquity measurement. Further, it is one of the youngest Neptunes/sub-Saturns in general with an obliquity constraint, only behind AU Mic c (H. Yu et al. 2025), V1298 Tau c (A. D. Feinstein et al. 2021), and TOI-5398 b (G. Mantovan et al. 2024; B. T. Radzom et al. 2024).

TOI-4507 b seems well suited for atmospheric characterization via transit spectroscopy. Assuming zero albedo, the expected equilibrium temperature of the planet is ∼460 K, lower than most other systems that have been subject to transit spectroscopy. Because of the planet's low density, the transmission spectroscopy metric (TSM; E. M. R. Kempton et al. 2018) is $\gtrsim$160. For reference, targets with TSM $>$ 90 are typically considered high-quality targets for atmospheric characterization. Observations with JWST might shed light on the atmospheric composition of TOI-4507 b and the origins of its unusually low density.

7.2. Search for Companions

Although there are no signs of additional transiting planets in the TESS light curve, there is evidence for a long-term RV trend. To discern whether this trend originates from an outer companion or is just a product of stellar activity, we calculated a series of stellar activity indicators using `serval` (M. Zechmeister et al. 2018) and the HARPS data, including the Hα index, the Na D I and II indices, the chromatic index, and the differential line width. The Hα index is the only one showing a (marginal) correlation with the derived RVs, having a Pearson correlation coefficient

Table 3
Summary of Priors and Posteriors of the RM-effect Fit

Parameter	Description	Prior	Posterior
λ	Sky-projected stellar obliquity (deg)	$\mathcal{U}(-180, 180)$	-15^{+50}_{-44}
$v \sin i_\star$	Projected rotational velocity (km s^{-1})	$\mathcal{U}(0, 15)$	$7.3^{+2.8}_{-1.8}$
$\rho_\star$	Stellar density (g cm^{-3})	$\mathcal{G}(1.41, 0.04)$	1.41 ± 0.04
P	Orbital period (days)	$\mathcal{G}(104.61611, 0.00006)$	104.61611 ± 0.00006
t_0	Transit midpoint (BJD)	$\mathcal{G}(2458413.8515, 0.0008)$	2458413.8514 ± 0.0008
b	Impact parameter	$\mathcal{G}(0.12, 0.08)$	$0.11^{+0.07}_{-0.06}$
$R_p/R_\star$	Radius ratio	$\mathcal{G}(0.0723, 0.0004)$	0.0723 ± 0.0004
$\sqrt{e}\,\sin\omega$	Eccentricity parameter sine component	$\mathcal{G}(-0.13, 0.06)$	-0.15 ± 0.06
$\sqrt{e}\,\cos\omega$	Eccentricity parameter cosine component	$\mathcal{G}(-0.09, 0.45)$	$-0.08^{+0.42}_{-0.37}$
e	Eccentricity	...	$0.11^{+0.20}_{-0.08}$
ω	Argument of periastron	...	-117^{+96}_{-46}
$q_1^{\rm HARPS}$	HARPS linear limb-darkening parameter	$\mathcal{U}(0, 1)$	$0.59^{+0.27}_{-0.31}$
$q_2^{\rm HARPS}$	HARPS quadratic limb-darkening parameter	$\mathcal{U}(0, 1)$	$0.65^{+0.25}_{-0.36}$
β	Intrinsic stellar line width (km s^{-1})	$\mathcal{G}(6.0, 2.0)$	$5.9^{+2.0}_{-2.1}$
$\gamma_{\rm HARPS}$	HARPS RV offset (m s^{-1})	$\mathcal{U}(25000, 27000)$	26068^{+9}_{-10}
$\dot{\gamma}_{\rm HARPS}$	HARPS RV slope (m s^{-1} day^{-1})	$\mathcal{U}(-200, 200)$	22^{+61}_{-63}
$\sigma_{\rm HARPS}$	HARPS RV jitter (m s^{-1})	$\mathcal{LU}(10^{-3}, 100)$	$1.8^{+3.7}_{-1.8}$

Note. $\mathcal{U}(a, b)$ denotes a uniform prior with a start value a and end value b. $\mathcal{G}(\mu, \sigma)$ denotes a normal prior with mean μ and standard deviation σ. $\mathcal{LU}(a, b)$ denotes a log-uniform prior with a start value a and end value b.

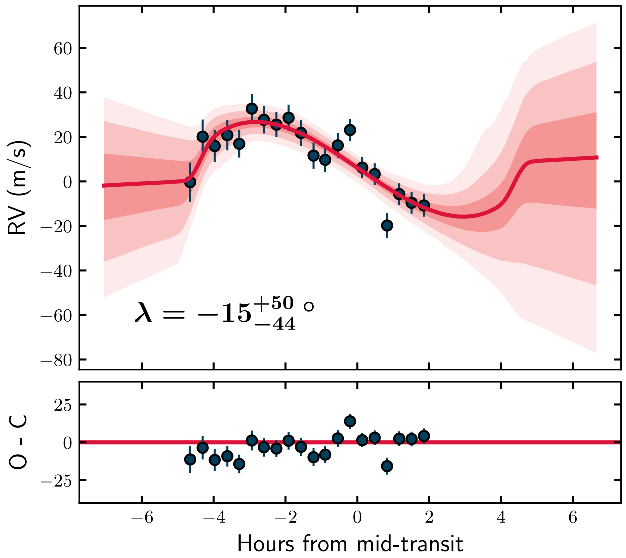

Figure 3. HARPS observations of the RM effect produced during the transit of TOI-4507 b, along with the best-fit model in red. The shaded areas show 1σ, 2σ, and 3σ models.

$r = 0.35 \pm 0.13$ and a $p-$ value $= 0.053^{+0.19}_{-0.05}$. Therefore, the hypothesis of stellar activity is disfavored.

If the RV trend is produced by a planetary companion, it should have an orbital period $P > 5.6$ yr, which corresponds to the baseline of the current RV observations. The parameters of this possible companion could be constrained with additional RV and/or Gaia DR4 and DR5 astrometric measurements. Although TOI-4507 is relatively massive, it is nearby ($d \approx 177$ pc) and bright ($G \approx 10.6$), so it is a good candidate for Gaia astrometric detections (e.g., M. Perryman et al. 2014; C. Lammers & J. N. Winn 2026). When removing the signal of TOI-4507 b and the RV trend from the data, we do not see clear additional signals in the RV data, which rules out the presence of planets producing similar or larger RV signals than TOI-4507 b.

In addition to planetary companions, we searched for potential stellar companions to TOI-4507. High-resolution imaging with SOAR rules out nearby sources within 3″ (Figure 2), corresponding to a projected separation of ∼530 au. This is further supported by the Gaia DR3 renormalized unit weight error of ∼0.8, which suggests that the astrometry is not significantly perturbed by an unresolved companion. On wider scales, TOI-4507 is not included in the wide binary catalog of K. El-Badry et al. (2021), which is based on proper motions and parallaxes from the Gaia Early DR3 (Gaia Collaboration et al. 2021), indicating the absence of comoving stellar companions within 1 pc. The available data then strongly support a single-star interpretation.

7.3. Explaining the Inferred Low Density

Next, we discuss some of the proposed explanations for the low-density planets.

Composition. One of the suggested hypotheses for explaining the low densities of some exoplanets is that they have unusually massive H/He envelopes relative to their small core masses, typically representing more than ∼20% of their total masses (e.g., E. D. Lopez & J. J. Fortney 2014; D. P. Thorngren et al. 2016). E. J. Lee & E. Chiang (2016) hypothesize that superpuff exoplanets might form in regions of their protoplanetary disks that are unusually cold and dust-free, then migrate to their currently observed orbits. This picture can explain their superpuffy nature and also the fact that many superpuffs are in or close to mean motion resonances (e.g., A. Leleu et al. 2024) if they experience slow convergent migration. Future observations of TOI-4507 with JWST can probe the atmospheric composition of the planet, which might confirm or rule out this hypothesis.

Tidal heating. An alternative hypothesis is that superpuff planets are inflated due to tidal heating produced by distortions

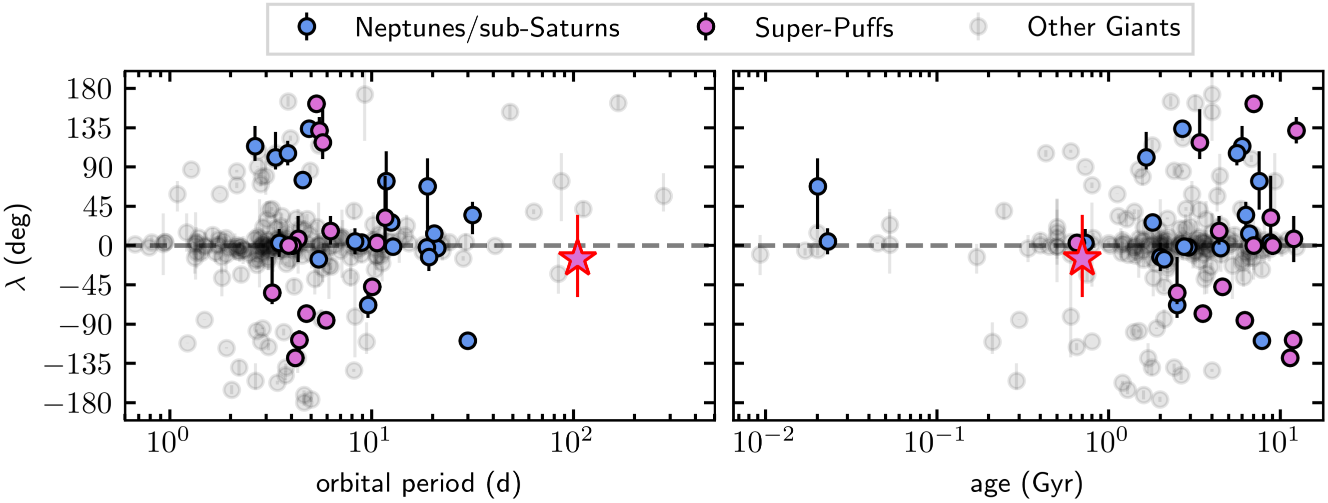

Figure 4. Sky-projected obliquity λ as a function of the orbital period (left) and age of the system (right). The population of Neptunes/sub-Saturns ($10 < M_p/M_\oplus < 90$) is shown in blue. Superpuff planets (Neptunes/sub-Saturns with $\rho_p < 0.3$ g cm^{-3}) are shown in pink, with TOI-4507 highlighted as a star with a red edge. Other giant-planet systems are shown as faint black points. The data are from TEPCat, with ages from the NASA Exoplanet Archive.

in the shape of the planet. These distortions are more pronounced the closer the planet orbits the star, as tidal forces become stronger (e.g., P. Hut 1981). S. Millholland (2019) and S. Millholland et al. (2020) showed that for planets in the Neptune regime, the radius can increase by up to a factor of ~2, possibly explaining the superpuffs. Indeed, most of the discovered superpuffs have short-period orbits and experience strong tidal forces, making this a valid explanation for them. However, this is not the case for TOI-4507 b, which has an orbital period of 105 days and does not experience significant tidal forces, making this scenario unlikely to explain its unusually low density.

Circumplanetary rings. One plausible explanation for the inferred superpuffy nature of some exoplanets with relatively long orbital periods is the idea of opaque rings around the planets (e.g., B. Akinsanmi et al. 2020; A. L. Piro & S. Vissapragada 2020; M. Saillenfest et al. 2023). Recently, T. Lu et al. (2025) showed that an optically thick ring system around HIP-41378 f could remain tilted, due to the planet's resonantly excited obliquity, thus explaining its unusually deep transit.

This scenario requires that the optically thick ring be both sustainable against Poynting–Robertson drag and maintained in a high-obliquity state. Regarding the first condition, K. Ohno & J. J. Fortney (2022) derived a critical equilibrium temperature above which a viscously evolving ring cannot persist:

$$T_{\rm crit} \sim 300\ {\rm K}\left(\frac{\rm Age}{0.7\ {\rm Gyr}}\right)^{-3/8}. \tag{1}$$

Since the planet's equilibrium temperature of $T_{\rm eq} \approx 460$ K is well above this threshold, the ring is unlikely to survive over the system's lifetime.

The second condition concerns the ring's obliquity. The radial extent over which a ring remains aligned with the planetary equator is set by the Laplace radius (R_L). For a planet with a rotationally induced quadrupolar moment J_2, this is

$$R_L \simeq \frac{2R_p}{3}\left(\frac{k_{2,p}}{0.4}\right)^{1/5}\left(\frac{P}{P_{\rm rot,p}}\right)^{2/5}, \tag{2}$$

where $P_{\rm rot,p}$ is the planetary spin period and $k_{2,p}$ is the Love number. For a planetary obliquity $\psi_{\rm p}$, the observed transit depth requires a projected ring area satisfying $R_L \sin\psi_{\rm p} \gtrsim 8\ R_\oplus$. In terms of the spin period, this condition becomes

$$P_{\rm rot} \lesssim 1.1\ {\rm days}\left(\frac{R_p}{4R_\oplus}\frac{1}{\sin\psi_{\rm p}}\right)^{5/2}. \tag{3}$$

Although subday rotation periods may be reasonable, or even expected, for a Neptune-like planet, the required values for rocky planets may approach the breakup rotation period (e.g., $P_{\rm rot} \lesssim 1$ hr for $R_p \lesssim 1.1\ R_\oplus$). Assuming instead a Neptune-like planet, the rotation must remain rapid, despite tidal damping. The corresponding spindown timescale is (e.g., A. C. M. Correia & J. Laskar 2010)

$$\tau_{\rm spin} \equiv \frac{P_{\rm rot,p}}{|\dot{P}_{\rm rot,p}|} \approx 0.7 \times 10^9\ {\rm yr}\left(\frac{Q_p/k_{2,p}}{10^5}\right)\left(\frac{M_p}{20M_\oplus}\right) \times \left(\frac{R_p}{4R_\oplus}\right)^{-3}\left(\frac{2}{1+\cos^2\psi_{\rm p}}\right), \tag{4}$$

which must exceed the system age (~0.7 Gyr). This condition implies a modified tidal quality factor $Q_p/k_{2,p} \gtrsim 10^5$, somewhat higher than the values inferred for Neptune and Uranus of $\sim 10^4$ (e.g., P. Goldreich & S. Soter 1966) but within the range of warm Neptunes based on eccentricity damping constraints (e.g., A. C. M. Correia et al. 2020).

In summary, the primary challenge for the ring hypothesis is that long-lived opaque rings are unlikely to survive at the planet's equilibrium temperature. If such rings were present, sustaining them in a high-obliquity configuration would require the planet to have a modified tidal quality factor of $Q_p/k_{2,p} \gtrsim 10^5$—a value that may be somewhat elevated but still plausible for a Neptune-like planet.

8. Conclusions

We have reported the discovery and characterization of TOI-4507 b, a transiting cold Neptune on a prograde orbit. With a radius of $8.2 \pm 0.1\,R_\oplus$, a mass $<20\,M_\oplus$, and a bulk density $<0.2\,\mathrm{g\,cm^{-3}}$, TOI-4507 b is among the longest-period ($P \sim 105$ days) superpuffs discovered to date. Further, TOI-4507 is one of the youngest Neptune/sub-Saturn systems with an obliquity constraint and one of the longest-period systems in general for which the obliquity has been measured.

The properties of TOI-4507 b raise important implications. Its unusually low density highlights the need to consider both compositional and structural explanations for superpuff planets, including massive H/He envelopes, inflation mechanisms, or obscuration by circumplanetary material. However, our analysis suggests that long-lived opaque rings are unlikely to survive at the planet's equilibrium temperature.

Given its brightness, young age, and extremely low density, TOI-4507 b is a prime target for follow-up studies. Transmission spectroscopy with JWST can test the superpuff hypothesis, by probing its atmospheric composition, while continued RV and astrometric monitoring can confirm the presence of an outer companion and further constrain the dynamical history of the system.

TOI-4507 thus joins a small but growing population of Neptune/sub-Saturn and superpuff systems with obliquity constraints, providing a valuable laboratory for understanding the formation, evolution, and diversity of planetary systems.

Acknowledgments

We would like to thank Yubo Su for suggesting the rotational constraint on the sizes of the rings. We also thank Yugo Kawai for kindly pointing out that the source of the variability observed in the TESS light curve of TOI-4507 is a blended variable star in the background and is not related to the rotational period of TOI-4507. We would also like to thank the anonymous referee for the thoughtful review and suggestions that improved the quality of this work. We also thank Songhu Wang, Xian-Yu Wang, and the Red Worlds Lab group at the University of Amsterdam for their useful discussions and suggestions that strengthened this manuscript.

J.I.E.-R. gratefully acknowledges support from the John and A-Lan Reynolds Faculty Research Fund, from the ANID BASAL project FB210003, and from the ANID Doctorado Nacional grant 2021-21212378.

R.B. acknowledges support from FONDECYT Project 1241963 and from ANID—Millennium Science Initiative—ICN12_009.

T.T. acknowledges support by the BNSF program "VIHREN-2021" project No. KP-06-DV/5.

Support for M.C. is provided by ANID's Millennium Science Initiative through grants ICN12_12009 and AIM23-001, awarded to the Millennium Institute of Astrophysics (MAS); by ANID/FONDECYT Regular grant 1231637; and by ANID/Basal (CATA) grant FB21003.

C.C. acknowledges support from ANID through FONDECYT post-doctoral grant No. 3230283.

A.V.F. acknowledges the support of the Institute of Physics through the Bell Burnell Graduate Scholarship Fund.

This Letter was based on observations collected at the European Southern Observatory under ESO programmes 0104.C-0413(A), 106.21ER.001, 112.25W1.001, 114.27CS.001, and 115.286G.001.

This Letter also made use of data collected by the TESS mission that are publicly available from the Mikulski Archive for Space Telescopes (MAST) operated by the Space Telescope Science Institute (STScI). Funding for the TESS mission is provided by NASA's Science Mission Directorate. We acknowledge the use of public TESS data from pipelines at the TESS Science Office and at the TESS Science Processing Operations Center. Resources supporting this work were provided by the NASA High-End Computing (HEC) Program through the NASA Advanced Supercomputing (NAS) Division at Ames Research Center for the production of the SPOC data products.

This work makes use of observations from the ASTEP telescope. ASTEP benefited from the support of the French and Italian polar agencies IPEV and PNRA in the framework of the Concordia station program and from OCA, INSU, Idex UCAJEDI (ANR- 15-IDEX-01), and ESA through the Science Faculty of the European Space Research and Technology Centre (ESTEC). This research also received funding from the European Research Council (ERC) under the European Union's Horizon 2020 research and innovation program (grant agreement No. 803193/BEBOP), from the Science and Technology Facilities Council (STFC; grant Nos. ST/S00193X/1, ST/W002582/1, and ST/Y001710/1), and from the ERC/UKRI Frontier Research Guarantee program (CandY/ EP/Z000327/1).

This work has been carried out within the framework of the National Centre of Competence in Research PlanetS supported by the Swiss National Science Foundation under grants 51NF40_182901 and 51NF40_205606.

This Letter is also based on observations obtained at the SOAR telescope, which is a joint project of the Ministério da Ciência, Tecnologia e Inovações (MCTI/LNA) do Brasil, the US National Science Foundation's NOIRLab, the University of North Carolina at Chapel Hill (UNC), and Michigan State University (MSU).

This research has made use of the Exoplanet Follow-up Observation Program (ExoFOP) and NASA Exoplanet Archive websites, which are operated by the California Institute of Technology under contract with NASA under the Exoplanet Exploration Program.

Data and Code Availability

A data package—containing the scripts used for the various analyses, the corresponding datasets, the results of each analysis, and Jupyter notebooks that reproduce the figures from the Letter—has been deposited to Zenodo: doi:10.5281/zenodo.17613518 (J. I. Espinoza-Retamal 2025). A copy of `ironman` version 1.1.0 is included. The complete set of RV measurements from HARPS, FEROS, and CORALIE is available in a machine-readable format in Table A1 in the Appendix.

Facilities: TESS, ASTEP, SOAR, ESO: 3.6m (HARPS), Max Planck: 2.2m (FEROS), Euler 1.2m (CORALIE), Exoplanet Archive, ExoFOP.

Software: `astropy` (Astropy Collaboration et al. 2013, 2018, 2022), `batman` (L. Kreidberg 2015), `celerite` (D. Foreman-Mackey et al. 2017), `ceres` (R. Brahm et al. 2017a), `dynesty` (J. S. Speagle 2020), `ironman` (J. I. Espinoza-Retamal et al. 2023a, 2024), `juliet` (N. Espinoza et al. 2019), `lightkurve` (Lightkurve Collaboration et al. 2018), `radvel` (B. J. Fulton et al. 2018), `rmfit` (G. Stefansson et al. 2022), `serval` (M. Zechmeister et al. 2018), `zaspe` (R. Brahm et al. 2017b).

Appendix A
RV Measurements

Table A1 shows the RVs of TOI-4507 taken with different instruments.

Table A1
RV Measurements from HARPS, FEROS, and CORALIE

BJD	RV (m s^{-1})	σ_{RV} (m s^{-1})	Instrument
2458717.932107	26,094.5	11.0	FEROS
2458718.898281	26,072.7	9.0	FEROS
2458722.879818	26,053.6	9.3	FEROS
…	…	…	…
2460667.658069	26,062.9	2.3	HARPS
2460692.667466	26,060.0	3.8	HARPS
2460744.564697	26,059.6	3.3	HARPS

(This table is available in its entirety in machine-readable form in the online article.)

Appendix B
Source of the Photometric Variability

As discussed in Section 4, the TESS light curve of TOI-4507 shows a clear modulation with periodicity of ∼1.7 days (see the upper panels of Figure B1). To investigate whether this variability is intrinsic to TOI-4507 (e.g., due to stellar rotation) or the result of contamination from blended sources in the TESS pixels, we checked archival Optical Gravitational Lensing Experiment (OGLE; A. Udalski et al. 1992) data of nearby sources. We identified a variable star, Gaia DR3 4657949658179626624, located at ∼32″ from TOI-4507, that shows variability with the same periodicity but with a larger amplitude (see the bottom panels of Figure B1). The variability amplitude of this neighboring source would translate to a variation consistent with the modulation observed in the blended TESS light curve. We then conclude that the variability observed in TESS is not related to TOI-4507 or its rotational period. Therefore, we are unable to constrain the stellar inclination and true 3D obliquity in the analysis.

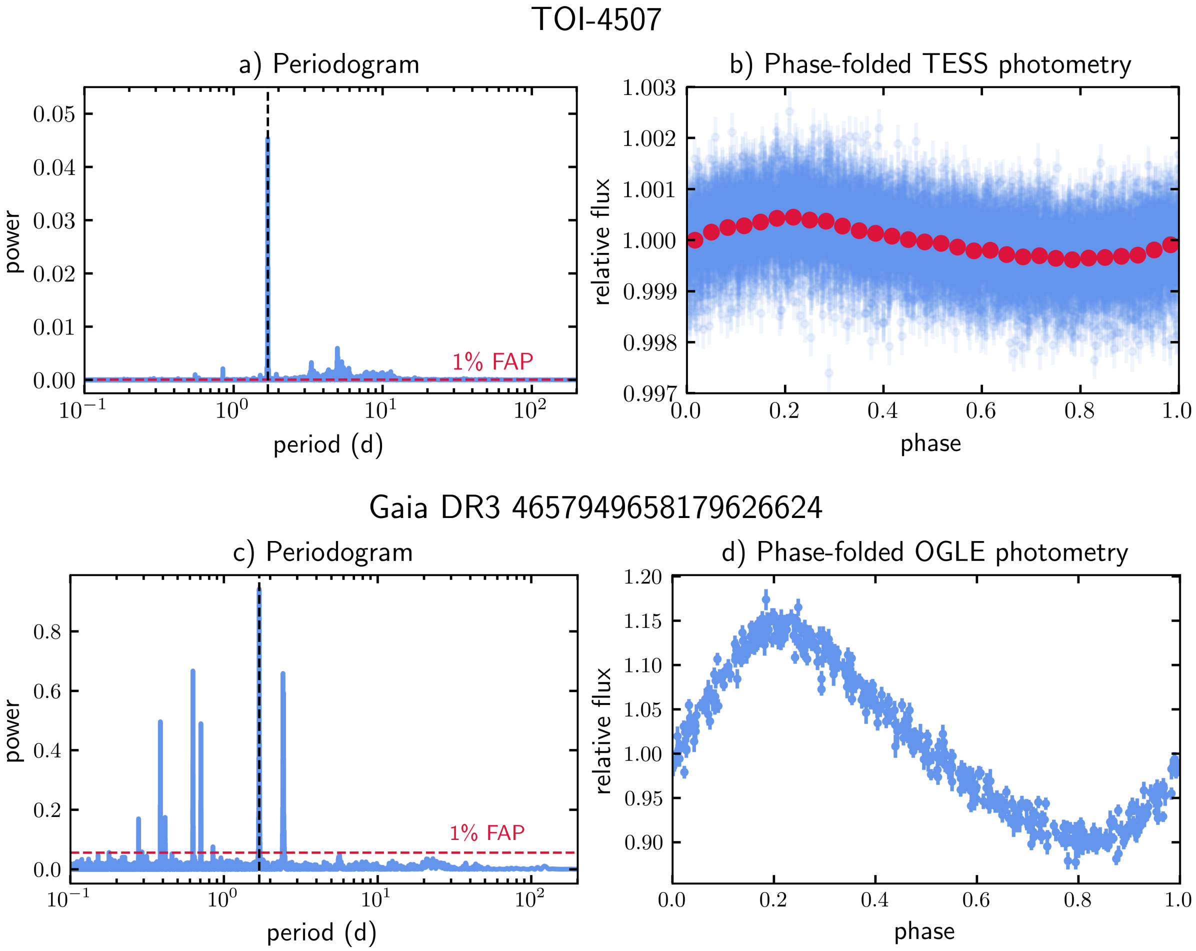

Figure B1. Observed modulation in the light curves of TOI-4507 (upper panels) and the nearby source Gaia DR3 4657949658179626624 (bottom panels). (a) Lomb–Scargle periodogram of the 2 minutes cadence TESS light curve of TOI-4507. A false-alarm probability (FAP) level of 1% is marked with a red dashed line. The black dashed line marks the highest-power peak, indicating a period of 1.7 days. (b) TESS light curve phased to the period of 1.7 days. All the work done here made use of the 2 minutes cadence light curve, but for illustrative purposes only, the 30 minutes cadence TESS light curve is shown here in blue, with the binned data in red. (c) Lomb–Scargle periodogram of the OGLE light curve of Gaia DR3 4657949658179626624, also showing a clear period of 1.7 days. (d) OGLE light curve of Gaia DR3 4657949658179626624 phased to the period of 1.7 days.

Appendix C
Corner Plot

Figure C1 shows the joint posterior distributions and histograms for some of the parameters of the RM fit described in Section 6.

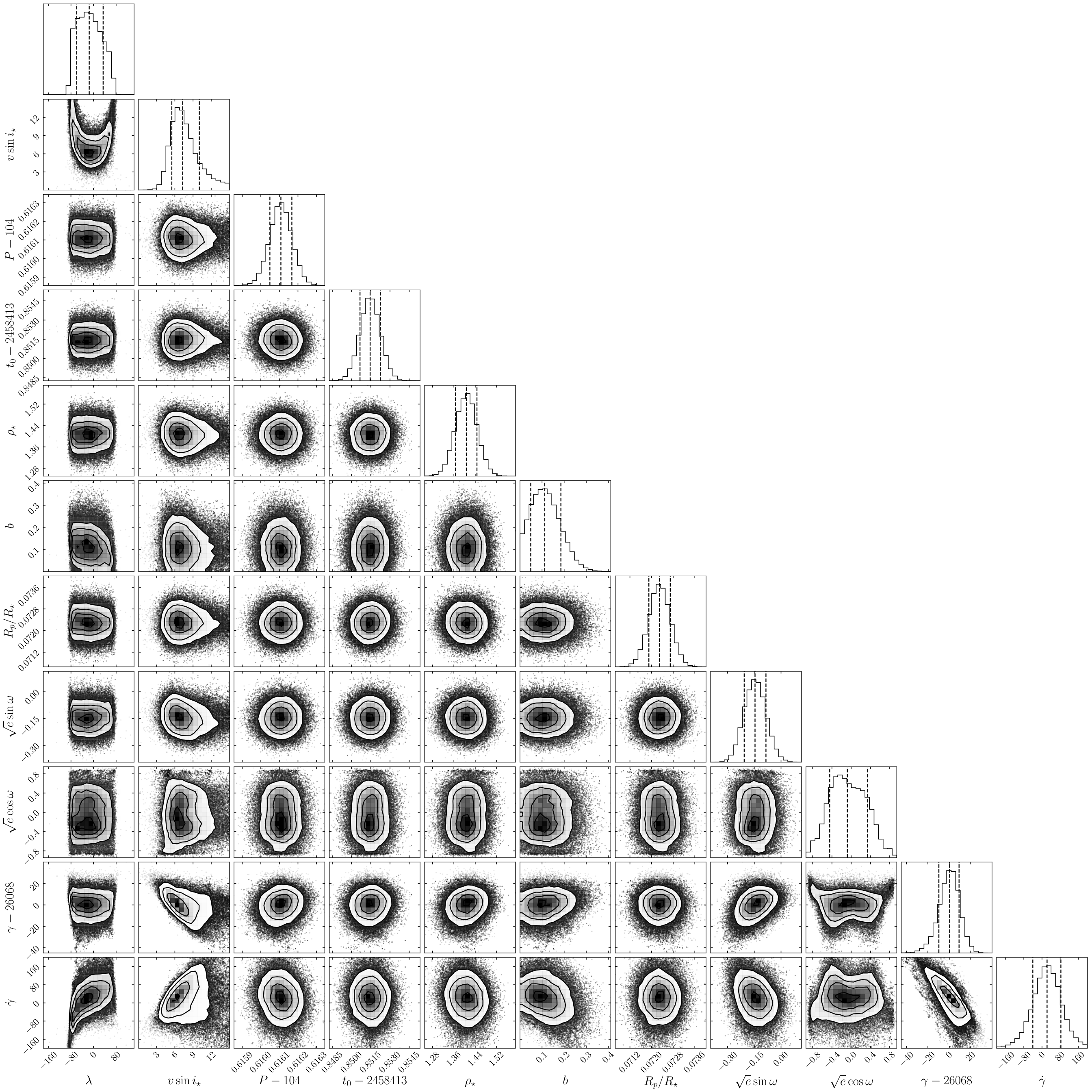

Figure C1. Joint posterior distributions and histograms of the posteriors for some of the parameters in our RM-effect model.

ORCID iDs

Juan I. Espinoza-Retamal https://orcid.org/0000-0001-9480-8526
Rafael Brahm https://orcid.org/0000-0002-9158-7315
Cristobal Petrovich https://orcid.org/0000-0003-0412-9314
Andrés Jordán https://orcid.org/0000-0002-5389-3944
Thomas Henning https://orcid.org/0000-0002-1493-300X
Trifon Trifonov https://orcid.org/0000-0002-0236-775X
Joshua N. Winn https://orcid.org/0000-0002-4265-047X
Erika Rea https://orcid.org/0009-0009-4849-9764
Maximilian N. Günther https://orcid.org/0000-0002-3164-9086
Abdelkrim Agabi https://orcid.org/0000-0001-7948-6493
Philippe Bendjoya https://orcid.org/0000-0002-4278-1437
Hareesh Bhaskar https://orcid.org/0000-0002-5181-0463
François Bouchy https://orcid.org/0000-0002-7613-393X
Márcio Catelan https://orcid.org/0000-0001-6003-8877
Carolina Charalambous https://orcid.org/0000-0002-9196-5734
Vincent Deloupy https://orcid.org/0009-0007-5876-546X
George Dransfield https://orcid.org/0000-0002-3937-630X
Jan Eberhardt https://orcid.org/0000-0003-3130-2768
Néstor Espinoza https://orcid.org/0000-0001-9513-1449
Alix V. Freckelton https://orcid.org/0009-0007-1053-0004
Tristan Guillot https://orcid.org/0000-0002-7188-8428
Melissa J. Hobson https://orcid.org/0000-0002-5945-7975
Monika Lendl https://orcid.org/0000-0001-9699-1459
Djamel Mekarnia https://orcid.org/0000-0001-5000-7292
Diego J. Muñoz https://orcid.org/0000-0003-2186-234X
Louise D. Nielsen https://orcid.org/0000-0002-5254-2499
Felipe I. Rojas https://orcid.org/0000-0003-3047-6272
François-Xavier Schmider https://orcid.org/0000-0003-3914-3546
Elyar Sedaghati https://orcid.org/0000-0002-7444-5315
Guđmundur Stefánsson https://orcid.org/0000-0001-7409-5688
Stephanie Striegel https://orcid.org/0009-0008-5145-0446
Olga Suarez https://orcid.org/0000-0002-3503-3617
Marcelo Tala Pinto https://orcid.org/0009-0004-8891-4057
Mathilde Timmermans https://orcid.org/0009-0008-2214-5039
Amaury H. M. J. Triaud https://orcid.org/0000-0002-5510-8751
Stéphane Udry https://orcid.org/0000-0001-7576-6236
Solène Ulmer-Moll https://orcid.org/0000-0003-2417-7006
Carl Ziegler https://orcid.org/0000-0002-0619-7639

References

Abe, L., Gonçalves, I., Agabi, A., et al. 2013, A&A, 553, A49
Akeson, R. L., Chen, X., Ciardi, D., et al. 2013, PASP, 125, 989
Akinsanmi, B., Santos, N. C., Faria, J. P., et al. 2020, A&A, 635, L8
Albrecht, S., Winn, J. N., Johnson, J. A., et al. 2012, ApJ, 757, 18
Astropy Collaboration, Price-Whelan, A. M., Lim, P. L., et al. 2022, ApJ, 935, 167
Astropy Collaboration, Price-Whelan, A. M., Sipőcz, B. M., et al. 2018, AJ, 156, 123
Astropy Collaboration, Robitaille, T. P., Tollerud, E. J., et al. 2013, A&A, 558, A33
Barkaoui, K., Pozuelos, F. J., Hellier, C., et al. 2024, NatAs, 8, 909
Bonomo, A. S., Dumusque, X., Massa, A., et al. 2023, A&A, 677, A33
Borucki, W. J., Koch, D., Basri, G., et al. 2010, Sci, 327, 977
Bourrier, V., Attia, M., Mallonn, M., et al. 2023, A&A, 669, A63
Brahm, R., Espinoza, N., Jordán, A., et al. 2019, AJ, 158, 45
Brahm, R., Jordán, A., & Espinoza, N. 2017a, PASP, 129, 034002
Brahm, R., Jordán, A., Hartman, J., & Bakos, G. 2017b, MNRAS, 467, 971
Brahm, R., Ulmer-Moll, S., Hobson, M. J., et al. 2023, AJ, 165, 227
Bressan, A., Marigo, P., Girardi, L., et al. 2012, MNRAS, 427, 127
Cardelli, J. A., Clayton, G. C., & Mathis, J. S. 1989, ApJ, 345, 245
Casasayas-Barris, N., Palle, E., Nowak, G., et al. 2017, A&A, 608, A135
Chen, G., Casasayas-Barris, N., Pallé, E., et al. 2020, A&A, 642, A54
Christiansen, J. L., McElroy, D. L., Harbut, M., et al. 2025, PSJ, 6, 186
Correia, A. C. M., Bourrier, V., & Delisle, J. B. 2020, A&A, 635, A37
Correia, A. C. M., & Laskar, J. 2010, in Exoplanets, ed. S. Seager (Univ. Arizona Press), 239, https://www.jstor.org/stable/j.ctt1814jx6
Cumming, A., Butler, R. P., Marcy, G. W., et al. 2008, PASP, 120, 531
Dransfield, G., Triaud, A. H. M. J., Guillot, T., et al. 2022, MNRAS, 515, 1328
Eberhardt, J., Trifonov, T., Henning, T., et al. 2025, AJ, 169, 298
El-Badry, K., Rix, H.-W., & Heintz, T. M. 2021, MNRAS, 506, 2269
Espinoza, N., Kossakowski, D., & Brahm, R. 2019, MNRAS, 490, 2262
Espinoza-Retamal, J. I. 2025, Data package for "A Cold and Super-Puffy Planet on a Prograde Orbit", v1, Zenodo, doi:10.5281/zenodo.17613518
Espinoza-Retamal, J. I., Brahm, R., Petrovich, C., et al. 2023a, ApJL, 958, L20
Espinoza-Retamal, J. I., Stefánsson, G., Petrovich, C., et al. 2024, AJ, 168, 185
Espinoza-Retamal, J. I., Zhu, W., & Petrovich, C. 2023b, AJ, 166, 231
Feinstein, A. D., Montet, B. T., Johnson, M. C., et al. 2021, AJ, 162, 213
Fernandes, R. B., Mulders, G. D., Pascucci, I., Mordasini, C., & Emsenhuber, A. 2019, ApJ, 874, 81
Foreman-Mackey, D., Agol, E., Angus, R., & Ambikasaran, S. 2017, AJ, 154, 220
Fulton, B. J., Petigura, E. A., Blunt, S., & Sinukoff, E. 2018, PASP, 130, 044504
Gaia Collaboration, Brown, A. G. A., Vallenari, A., et al. 2021, A&A, 649, A1
Gaia Collaboration, Vallenari, A., Brown, A. G. A., et al. 2023, A&A, 674, A1
Gaudi, B. S., Seager, S., & Mallen-Ornelas, G. 2005, ApJ, 623, 472
Goldreich, P., & Soter, S. 1966, Icar, 5, 375
Gray, D. F. 1984, ApJ, 281, 719
Grouffal, S., Santerne, A., Bourrier, V., et al. 2022, A&A, 668, A172
Guillot, T., Abe, L., Agabi, A., et al. 2015, AN, 336, 638
Gupta, A. F., Millholland, S. C., Im, H., et al. 2024, Natur, 632, 50
Handley, L. B., Howard, A. W., Rubenzahl, R. A., et al. 2025, AJ, 169, 212
Hébrard, G., Désert, J. M., Díaz, R. F., et al. 2010, A&A, 516, A95
Hirano, T., Suto, Y., Taruya, A., et al. 2010, ApJ, 709, 458
Hut, P. 1981, A&A, 99, 126
Jenkins, J. M., Twicken, J. D., McCauliff, S., et al. 2016, SPIE, 9913, 99133E
Kaufer, A., Stahl, O., Tubbesing, S., et al. 1999, Msngr, 95, 8
Kempton, E. M. R., Bean, J. L., Louie, D. R., et al. 2018, PASP, 130, 114401
Kipping, D. M. 2013, MNRAS, 435, 2152
Knudstrup, E., Albrecht, S. H., Winn, J. N., et al. 2024, A&A, 690, A379
Kreidberg, L. 2015, PASP, 127, 1161
Lammers, C., & Winn, J. N. 2026, AJ, 171, 18
Lee, E. J., & Chiang, E. 2016, ApJ, 817, 90
Leleu, A., Delisle, J.-B., Burn, R., et al. 2024, A&A, 687, L1
Lendl, M., Triaud, A. H. M. J., Anderson, D. R., et al. 2014, A&A, 568, A81
Lightkurve Collaboration, Cardoso, J. V. d. M., Hedges, C., et al., 2018 Lightkurve: Kepler and TESS time series analysis in Python, Astrophysics Source Code Library, ascl:1812.013
Lopez, E. D., & Fortney, J. J. 2014, ApJ, 792, 1
Lu, T., Li, G., Cassese, B., & Lin, D. N. C. 2025, ApJ, 980, 39
Mancini, L., Esposito, M., Covino, E., et al. 2018, A&A, 613, A41
Mantovan, G., Malavolta, L., Locci, D., et al. 2024, A&A, 684, L17
Masuda, K. 2014, ApJ, 783, 53
Mayor, M., Pepe, F., Queloz, D., et al. 2003, Msngr, 114, 20
McLaughlin, D. 1924, ApJ, 60, 22
Mékarnia, D., Guillot, T., Rivet, J. P., et al. 2016, MNRAS, 463, 45
Millholland, S. 2019, ApJ, 886, 72
Millholland, S., Petigura, E., & Batygin, K. 2020, ApJ, 897, 7
Munari, U., Henden, A., Frigo, A., et al. 2014, AJ, 148, 81
Ohno, K., & Fortney, J. J. 2022, ApJ, 930, 50
Perryman, M., Hartman, J., Bakos, G. Á., & Lindegren, L. 2014, ApJ, 797, 14
Piro, A. L., & Vissapragada, S. 2020, AJ, 159, 131
Queloz, D., Mayor, M., Udry, S., et al. 2001, Msngr, 105, 1
Radzom, B. T., Dong, J., Rice, M., et al. 2024, AJ, 168, 116
Rea, E., Günther, M. N., Dransfield, G., et al. 2025, arXiv:2510.01725
Ricker, G. R., Winn, J. N., Vanderspek, R., et al. 2015, JATIS, 1, 014003
Rossiter, R. 1924, ApJ, 60, 15
Saillenfest, M., Sulis, S., Charpentier, P., & Santerne, A. 2023, A&A, 675, A174
Santerne, A., Malavolta, L., Kosiarek, M. R., et al. 2019, arXiv:1911.07355
Sebring, T. A., Krabbendam, V. L., & Heathcote, S. R. 2003, SPIE, 4837, 71
Sethi, R., & Millholland, S. 2025, ApJ, 988, 247

Skrutskie, M. F., Cutri, R. M., Stiening, R., et al. 2006, AJ, 131, 1163
Smith, J. C., Stumpe, M. C., Van Cleve, J. E., et al. 2012, PASP, 124, 1000
Southworth, J. 2011, MNRAS, 417, 2166
Speagle, J. S. 2020, MNRAS, 493, 3132
Stassun, K. G., Oelkers, R. J., Paegert, M., et al. 2019, AJ, 158, 138
Stassun, K. G., Oelkers, R. J., Pepper, J., et al. 2018, AJ, 156, 102
Stefansson, G., Mahadevan, S., Maney, M., et al. 2020, AJ, 160, 192
Stefansson, G., Mahadevan, S., Petrovich, C., et al. 2022, ApJL, 931, L15
Stumpe, M. C., Smith, J. C., Catanzarite, J. H., et al. 2014, PASP, 126, 100
Stumpe, M. C., Smith, J. C., Van Cleve, J. E., et al. 2012, PASP, 124, 985
Tala Pinto, M., Jordán, A., Acuña, L., et al. 2025, A&A, 694, A268
Tayar, J., Claytor, Z. R., Huber, D., & van Saders, J. 2022, ApJ, 927, 31
Thorngren, D. P., Fortney, J. J., Murray-Clay, R. A., & Lopez, E. D. 2016, ApJ, 831, 64
Tokovinin, A. 2018, PASP, 130, 035002
Udalski, A., Szymanski, M., Kaluzny, J., Kubiak, M., & Mateo, M. 1992, AcA, 42, 253
Vanderburg, A., Becker, J. C., Kristiansen, M. H., et al. 2016, ApJL, 827, L10
Vítková, M., Brahm, R., Trifonov, T., et al. 2025, ApJL, 978, L22
Wittenmyer, R. A., Butler, R. P., Tinney, C. G., et al. 2016, ApJ, 819, 28
Yee, S. W., Stefánsson, G., Thorngren, D., et al. 2025, AJ, 169, 225
Yu, H., Garai, Z., Cretignier, M., et al. 2025, MNRAS, 536, 2046
Zechmeister, M., Reiners, A., Amado, P. J., et al. 2018, A&A, 609, A12
Zhu, W., & Dong, S. 2021, ARA&A, 59, 291
Ziegler, C., Tokovinin, A., Briceño, C., et al. 2020, AJ, 159, 19